



# A hybrid approach to improve microstructure and mechanical properties of cold spray additively manufactured A380 aluminum composites

Xiang Qiu <sup>a,b</sup>, Naeem ul Haq Tariq <sup>c</sup>, Lu Qi <sup>a,b</sup>, Ji-Qiang Wang <sup>a,\*</sup>, Tian-Ying Xiong <sup>a,\*\*</sup>

<sup>a</sup> Institute of Metal Research, Chinese Academy of Sciences, Shenyang, 110016, China

<sup>b</sup> School of Materials Science and Engineering, University of Science and Technology of China, Shenyang, 110016, China

<sup>c</sup> Department of Metallurgy and Materials Engineering, Pakistan Institute of Engineering and Applied Sciences, Nilore, Islamabad, Pakistan



## ARTICLE INFO

### Keywords:

Cold spray additive manufacturing  
 $\text{Al}_2\text{O}_3$  particles  
 Heat-treatment  
 Microstructure  
 Mechanical properties

## ABSTRACT

This study comprehensively determined the microstructure and mechanical properties of cold spray additively manufactured A380 alloy components. In this regard, three types of  $\text{Al}_2\text{O}_3/\text{A}380$  composite deposits were prepared by separately mixing spherical, irregular, and spherical + irregular shaped  $\text{Al}_2\text{O}_3$  particulates with the original A380 alloy powder. The as-sprayed deposits were subsequently subjected to heat-treatment at 350 °C for 4 h. The effects of  $\text{Al}_2\text{O}_3$  morphology on the microstructure and mechanical properties of A380 deposits were systematically investigated at different processing stages by electron backscattered diffraction analysis and tensile testing, respectively. Moreover, the evolution of defects (pores and dislocation) inside the deposits was comprehensively studied using X-ray computed tomography and transmission electron microscopy techniques. The results indicated that the deposit containing spherical  $\text{Al}_2\text{O}_3$  exhibited significantly reduced porosity, grain refinement and a significant increase in strength (~70%) in contrast to the pure A380 alloy deposit. This could be attributed to the tamping effect of the spherical  $\text{Al}_2\text{O}_3$  particles. In contrast, the irregular  $\text{Al}_2\text{O}_3$  particles primarily indicated the embedding effect with recurrence of fragmentation events inside the deposit. Consequently, the deposit containing irregular  $\text{Al}_2\text{O}_3$  indicated only a slight decrease in porosity and a ~40% increase in strength in contrast to the pure A380 alloy deposit. The tensile test results indicated that heat-treatment significantly improved the plasticity of deposits through fusion of nano-sized pores, reduction in dislocation density and static re-crystallization. Therefore, the hybrid approach of adding a suitable tamping aid to the original A380 alloy powder and post-spray heat-treatment optimized the microstructure of cold spray additively manufactured components to significantly improve their mechanical properties.

## 1. Introduction

In recent years, additive manufacturing (AM) has emerged as an important manufacturing technology across multiple industries such as automotive, biomedical and aerospace [1,2]. Generally, AM utilizes laser and electron beams to construct a component layer-by-layer with the aid of a computer aided design (CAD) model [3,4]. Thus, AM increases manufacturing flexibility through fabrication of complex geometries and enhancement of product customization. However, AM has been successfully executed only for a few alloys (such as Ni based alloys, Ti6Al4V, Inconel 718, and AlSi10Mg) and most of the commonly used alloys cannot be printed reliably for various reasons [1]. For example, melting and solidification dynamics result in undesired micro-cracks

during 3D printing of high-strength Al or Mg alloys [3]. Moreover, high-reflectivity metals and alloys, such as those of copper and aluminum, are challenging to process using laser based AM [5]. Therefore, it is imperative to explore alternative AM technologies to meet the fabrication requirements of different materials.

Cold spray (CS) technology has been recently introduced as a promising AM method for fabricating freestanding metal components due to its unique solid-state fabrication principle. During the CS process, feedstock particles are mixed with an inert gas stream at the inlet of a converging diverging type nozzle to form a high velocity jet [6]. Subsequently, the feedstock particles impact on the substrate with supersonic speed and deposition is achieved through severe plastic deformation of the metallic particles. Contrary to traditional AM

\* Corresponding author.

\*\* Corresponding author.

E-mail addresses: [jqwang11s@imr.ac.cn](mailto:jqwang11s@imr.ac.cn) (J.-Q. Wang), [txiong@imr.ac.cn](mailto:txiong@imr.ac.cn) (T.-Y. Xiong).

techniques, the temperature of feedstock particles is maintained significantly below their melting point throughout the CS process [7,8]. Consequently, issues such as oxidation, phase transformation, evaporation and grain growth are minimized [9]. Moreover, thermal residual stresses in the deposits are effectively avoided due to low heat input. Subsequently, crack-free metallic deposits with virtually no limitation in the thickness can be fabricated [3].

Therefore, cold spray additive manufacturing (CSAM) has emerged as a suitable technique for fabricating temperature-sensitive materials (such as nano-crystalline materials) as well as Al and Mg-based alloys characterized by low melting temperatures [10–12]. Currently, CSAM has been successfully employed to fabricate components with rotational symmetry such as cylinder walls and tubes. Moreover, fabrication of components with complex geometry structures (e.g., fin array heat sinks, metal 2D codes, and metallic labels) has also been accomplished by utilizing a suitable mandrel, spindle, or mask [5,13].

However, CSAM is an emerging technique and exhibits limitations in the manufacture of engineering materials. In particular, the feedstock powder is deposited in solid state and most metallic particles are combined through mechanical interlocking, thus resulting in inherent defects (micro-pores and cracks) and poor inter-splat bonding [5,14]. Moreover, cold spray additively manufactured components in as-sprayed state exhibit brittle behavior due to severe work hardening. Consequently, cold spray additively manufactured components exhibit poor mechanical properties. Recent studies have focused on altering the microstructure of cold-sprayed deposits to improve their mechanical properties. For example, post-spray heat-treatment is a widely used method to effectively eliminate residual stresses in deposits through recovery and re-crystallization [15–17]. However, it has been reported that heat-treatment can heal only a limited number of pores/defects existing at the inter-splat boundaries of porous deposits characterized by numerous internal defects [17]. In our previous work, we fabricated an A380 (Al-Si-Cu alloy) cylinder using the CSAM technique [18]. Subsequently, the cylinder was subjected to a series of heat-treatments to investigate its microstructure evolution and mechanical properties. The results indicated that the heat-treatments induced a limited reduction in porosity as well as augmentation of pores in the vicinity of splat boundaries, which adversely affected the mechanical properties of the A380 alloy deposit [18]. Therefore, the simple post-spray heat-treatment resulted in marginal effects with regard to modifying the microstructure of deposits. Thus, fabrication of high quality components by CSAM with effective control of defect formation needs further investigation. Recent studies have reported that addition of hard particles, such as Al<sub>2</sub>O<sub>3</sub> [19,20], SiC [21], and TiN [22], into the feedstock powder can increase the compactness of final deposits, thereby reducing defect distributions in the deposits. Li et al. [22] studied the characteristics of CS-fabricated TiN/Al2319 composite deposits. The results indicated that the angular TiN particles played a pinning role in the matrix and resulted in reduced porosity as well as increased cohesive strength of the composite in contrast to pure Al2319 alloy deposit. A recent study introduced the “in-situ micro-forging effect” to the CSAM where large sized (100–200 µm) spherical particles were added to the metallic feedstock powder to achieve the hammering effect during deposition of the Inconel 718 alloy [11]. In-situ micro-forging significantly decreased the porosity of the deposit and improved the inter-splat bonding. Consequently, the mechanical properties of the deposit were significantly improved. Similarly, our previous work comprehensively investigated the effects of hard particle morphology on the microstructure of cold sprayed Al<sub>2</sub>O<sub>3</sub>/A380 composite deposits [14]. The results indicated that spherical Al<sub>2</sub>O<sub>3</sub> particles exhibited micro-tamping effect and few particles were retained in the final deposits. Consequently, the deposits exhibited low porosity, low surface roughness and improved interface bonding. In contrast, irregular Al<sub>2</sub>O<sub>3</sub> particles showed embedding effect during the CS process and significantly higher deposition efficiency, thus resulting in high hardness, high surface roughness, and relatively high porosity of the deposit. These studies provide novel insights for

improving the internal structure of cold sprayed components and a theoretical basis for improving the mechanical properties by mixing hard particles (with different morphologies) with the feedstock powder. To the best of our knowledge, no study has demonstrated the effects of hard particle morphology on the mechanical properties of cold sprayed components.

Therefore, this study attempted to control the microstructure and mechanical properties of cold spray additively manufactured A380 alloy components through a hybrid approach, i.e., (i) addition of dissimilar Al<sub>2</sub>O<sub>3</sub> particles to the A380 alloy feedstock → (ii) conducting CSAM → (iii) post-spray heat-treatment. The effects of morphology of Al<sub>2</sub>O<sub>3</sub> particles on the microstructure and mechanical properties of A380 deposits were systematically investigated at different processing stages by electron backscattered diffraction (EBSD) analysis and tensile test, respectively. Finally, the impact of heat-treatment on the evolution of defects (pores and dislocation) inside the deposits was studied using the X-ray computed tomography (XCT) and transmission electron microscopy (TEM) techniques.

## 2. Materials and methods

### 2.1. Raw material

Spherical gas atomized A380 alloy powder (chemical composition (wt.%): 8.74% Si, 3.30% Cu, 0.35% Zn, 0.27% Fe, and Al (balance)) was selected as the matrix material while Al<sub>2</sub>O<sub>3</sub> particulates with spherical and irregular morphologies, were used as the particulate phase. Further details on these as-received powders can be found elsewhere [14]. Three batches of feedstock were prepared with the following formulations: (i) 20 wt% spherical Al<sub>2</sub>O<sub>3</sub> powder + 80 wt% A380 alloy powder ((S) composite deposit), (ii) 20 wt% irregular Al<sub>2</sub>O<sub>3</sub> powder + 80 wt% A380 alloy powder ((I) composite deposit), and (iii) 10 wt% spherical Al<sub>2</sub>O<sub>3</sub> powder + 10 wt% irregular Al<sub>2</sub>O<sub>3</sub> powder + 80 wt% A380 alloy powder ((S + I) composite deposit). A commercially available 6061 aluminum alloy plate (dimensions: 50 × 50 × 3 mm<sup>3</sup>) was used as the substrate material. Further, the substrate was cleaned with acetone and subsequently sandblasted to remove the surface oxide layer before executing the CS process.

### 2.2. Sample preparation

Feedstock powders were cold sprayed layer-by-layer on a 6061 Al alloy substrate using the PCS-1000 cold spray system (Plasma Giken Co., Ltd., Japan) operated at ~500 °C with a gas pressure of 4 MPa. Nitrogen was used as the carrier and propelling gas. A constant standoff distance of 30 mm was maintained throughout the experiment. Traverse speed of the spraying nozzle was set to 100 mm/s while the powder feed rate was maintained at 25 ± 5 g/min during the entire process. Deposits with ~5mm thickness were obtained for all feedstock formulations. Subsequently, electrical discharge machining was used to carefully remove the substrate from the composite. Further, the free-standing composite specimens (dimensions: 45 × 35 × 5 mm<sup>3</sup>) were sectioned for microstructural characterization and post-spray heat-treatment. Thereafter, the samples were subjected to heat-treatment (at 350 °C for 4 h) in a muffle furnace to remove the work hardening effect and improve the splat bonding in the composites. Fig. 1 presents each processing step of the CSAM as well as the subsequent heat-treatment. Further, the tensile test specimens were cut in the plane parallel to the deposition surface to evaluate mechanical properties of the as-sprayed and heat-treated samples (Fig. 1). The tensile tests were performed on a universal testing machine (INSTRON 5848, UK). Detailed information regarding the test parameters and sample dimensions can be found elsewhere [23].

### 2.3. Microstructural characterization

The microstructural changes at different processing steps were

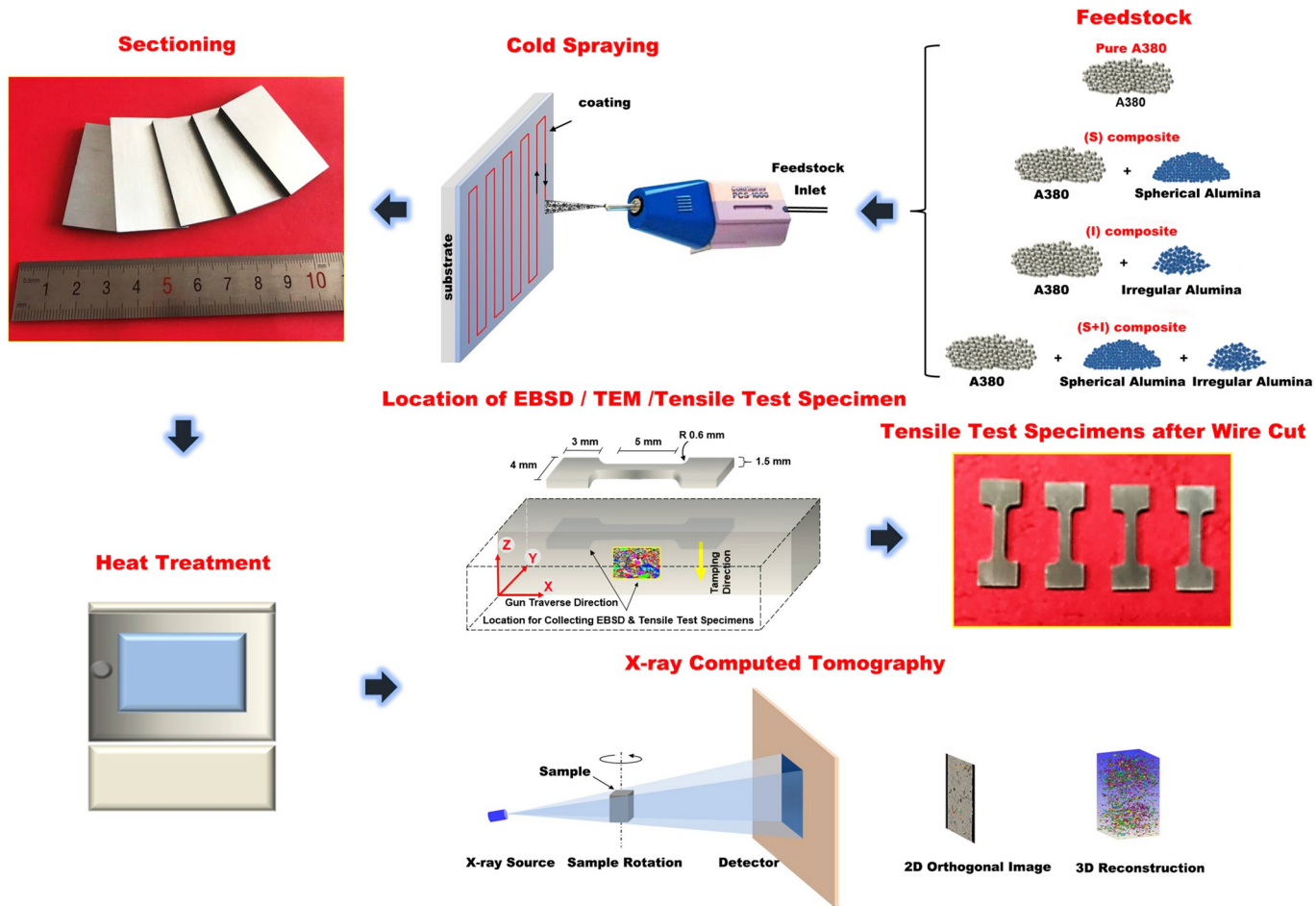


**Fig. 1.** Schematic of the cold spray process, post-spray heat-treatment, and characterization of the deposits.

examined using an scanning electron microscopy (SEM, Zeiss Merlin Compact, Germany) attached to the EBSD system. For the EBSD analysis, samples were cut from the central region of the as-sprayed and heat-treated deposits at directions parallel to the spray gun traverse direction (i.e., X direction) and the particle impact direction (i.e., Z direction). Samples were prepared using the standard metallographic procedure followed by vibration polishing with 50 nm silica suspensions for 8 h. During the EBSD test, samples were scanned in the X-Z plane with a step size of 150 nm. After the EBSD scanning, the Oxford Instruments Channel-5 software was employed to analyze the raw data. Additionally, TEM (Tencai T20, Japan) was used to elucidate the interface and sub-structural information for samples under different conditions.

#### 2.4. XCT analysis

A three-dimensional (3-D) XCT (XRM-500, Carl Zeiss X-ray Microscopy Inc., USA) was used to precisely study the size, distribution, and morphology of pores formed in the deposits during different processing conditions. Cylindrical samples (dimensions:  $\Phi 0.6 \times 4 \text{ mm}^3$ ) were machined and placed on a 360° rotation stage in front of the X-ray source as illustrated in Fig. 1. The accelerating voltage was set to 50 kV for all XCT experiments. Further, a cubic volume (dimensions:  $400 \times 400 \times 400 \mu\text{m}^3$ ) was selected from the scanned sample (voxel size:  $1.3 \times 1.3 \times 1.3 \mu\text{m}^3$ ) for subsequent analysis. The 3-D reconstruction maps were plotted using the Avizo software (V7.1, Visualization Sciences Group, Bordeaux, France).

## 3. Results

### 3.1. Microstructural analysis

#### 3.1.1. Cross-sectional characterization of as-sprayed deposits

Fig. 2 presents the cross-sectional SEM images for the as-sprayed deposits. Pore size for the pure A380 alloy deposit was  $\sim 5 \mu\text{m}$  which indicated insufficient deformation of the A380 particles during the

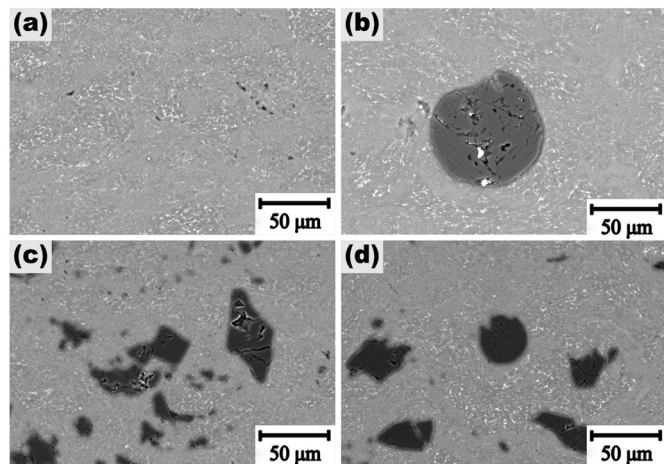


**Fig. 2.** Cross-sectional SEM images of (a) pure A380 alloy deposit, (b) (S) composite deposit, (c) (I) composite deposit, and (d) (S + I) composite deposit.

deposition process. Consequently, defects were formed at the splat boundaries. On the other hand, the composite deposits indicated relatively dense microstructure and absence of pores. Compared with 14.9 vol% of  $\text{Al}_2\text{O}_3$  in the feedstock, the average  $\text{Al}_2\text{O}_3$  content, (as estimated by Image J software), in the (S), (I) and (S + I) composite deposits was 2.1, 13.2, and 6.8 vol%, respectively. Further, the (I) composite deposit showed large amount of fragmented/cracked  $\text{Al}_2\text{O}_3$  particles.

### 3.1.2. XCT analysis

Small-sized pores located at the splat boundaries could not be resolved in the SEM images because the soft matrix material has sheared over the pores during the grinding operation. Consequently, the porosity values estimated by the SEM image analysis were not totally accurate. Therefore, XCT was utilized to precisely study the size, morphology, and distribution of pores inside the deposits under different processing conditions. Figs. 3 and 4 present the distribution of internal pores and porosity values for deposits in as-sprayed and heat-treated conditions, respectively. It should be noted that the data presented in Figs. 3 and 4 were obtained from the “in-situ” observation of pores. Additionally, the same location was utilized for performing XCT analysis before and after the heat-treatment. Subsequently, the pores were color coded according to the equivalent diameter (i.e., spherical diameter of an object with equal voxel volume) by utilizing the reconstruction process. Fig. 4 indicates that pure A380 had the highest porosity (~1.3%) among all four as-sprayed deposits. Further, the effect of addition of different morphologies of  $\text{Al}_2\text{O}_3$  on the porosity of deposits varies significantly. The porosity of (I) composite deposit decreased slightly while (S) and (S + I) composite deposits exhibited significantly lower porosity values (i.e., ~0.6 and 0.8%, respectively). Moreover, the heat-treatment enhanced porosity to simultaneously increase the number and size of pores in all the deposits (Fig. 3). This is inconsistent with previous studies [11]. The effect of  $\text{Al}_2\text{O}_3$  morphology on pore characteristics will be discussed in section 4.1.

### 3.1.3. EBSD analysis

Fig. 5 presents the color-coded inverse pole figures (IPF) superimposed on the band contrast images of different samples for as-sprayed and heat-treated conditions. Fig. 6 presents the corresponding average grain size of the matrix as measured by the Channel 5 software. The un-indexed regions (indicated by arrows in Fig. 5) in the as-sprayed deposits

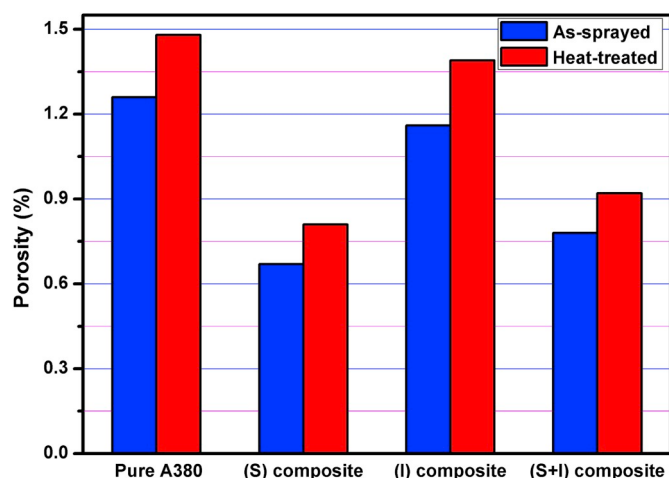


Fig. 4. Porosity of different samples for as-sprayed and heat-treated conditions.

were primarily located at the edge of the severely deformed splats, thus indicating that fine grains of size less than the scanning step size (150nm) were produced [24–26]. In contrast to grains in the pure A380 alloy deposit, the addition of both types of  $\text{Al}_2\text{O}_3$  (i.e., spherical and irregular) particulates resulted in significant grain refinement in the A380 matrix. This is evident in Fig. 5(b–d) which indicates that thin-strip grains with an average size of ~0.7  $\mu\text{m}$  were uniformly distributed throughout the samples. Further, the splat boundaries merged and were nearly indistinguishable after the heat-treatment. Moreover, regions that underwent severe plastic deformation disappeared. Consequently, a homogeneous microstructure with evenly distributed equiaxed grains was obtained. The average grain size of heat-treated samples (>0.9  $\mu\text{m}$ ) was slightly higher than that of as-sprayed deposits.

Fig. 7 presents the kernel average misorientation (KAM) maps of different samples for as-sprayed and heat-treated conditions. The KAM maps were generated by calculating the average mis-orientation of a point with respect to its first nearest neighbors. Mis-orientations > 5° were not considered in the KAM calculations. As indicated in Fig. 7(a), a dense network of dislocations/local strains was uniformly distributed in

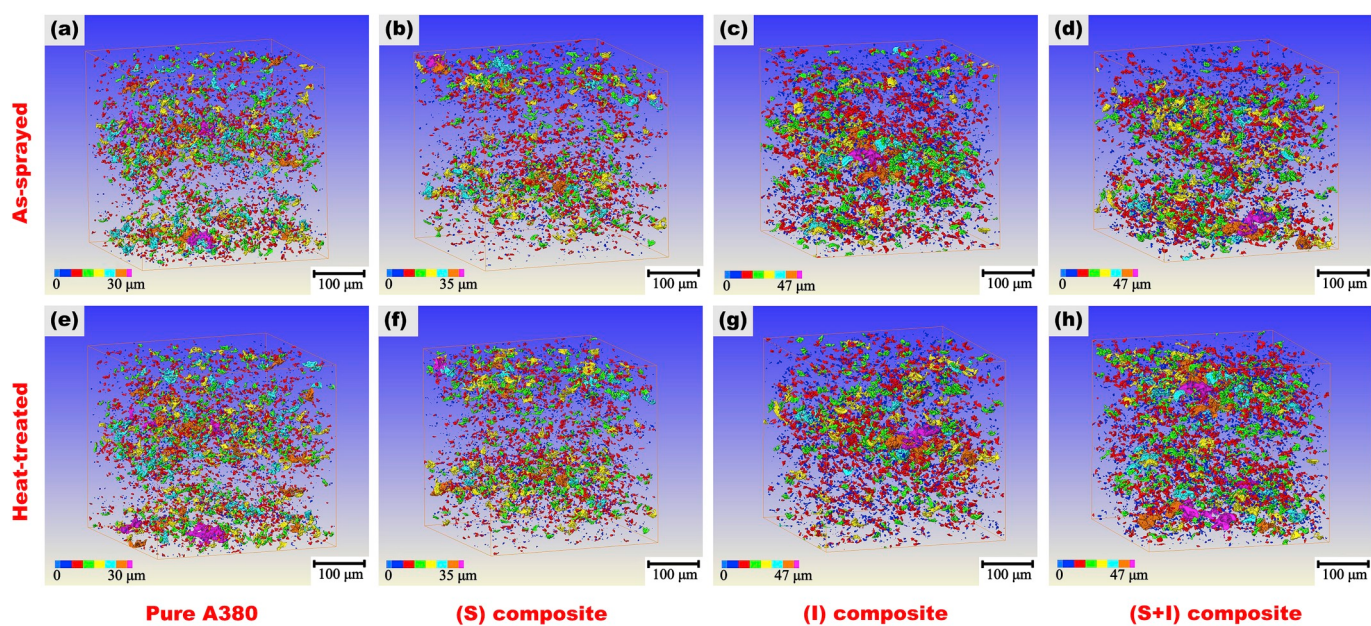
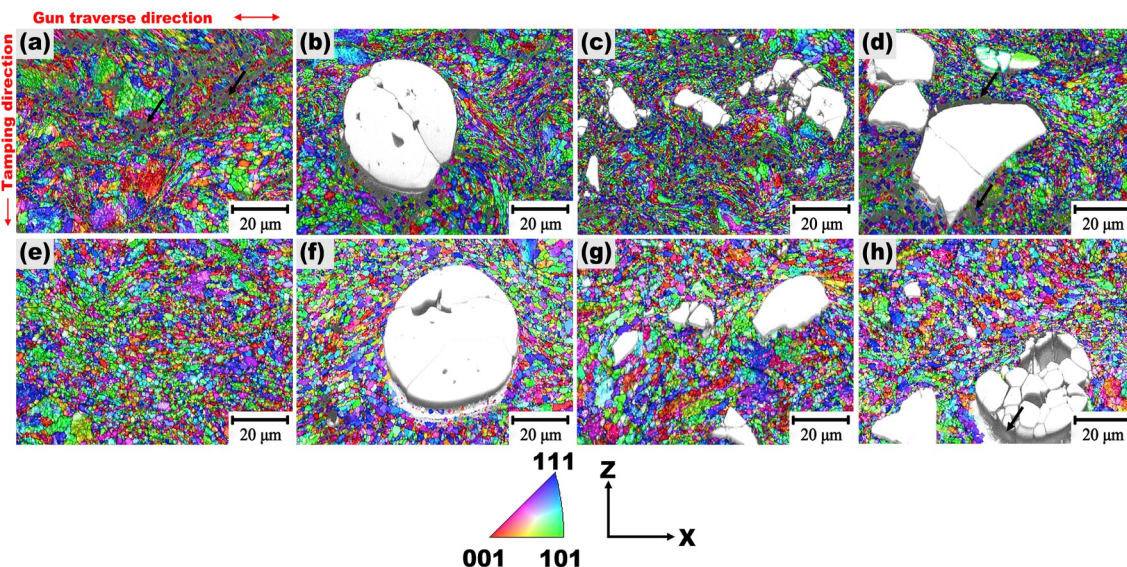
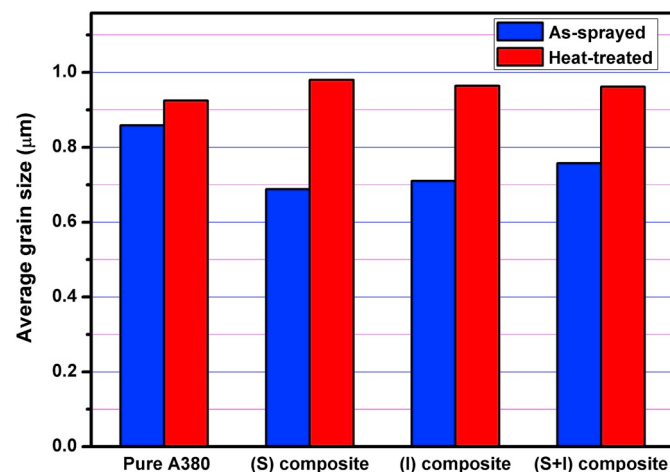


Fig. 3. 3-D reconstruction of pores for different samples in as-sprayed and heat-treated conditions: (a, e) pure A380 alloy deposit, (b, f) (S) composite deposit, (c, g) (I) composite deposit, and (d, h) (S + I) composite deposit.



**Fig. 5.** IPF maps of different samples for as-sprayed and heat-treated conditions: (a, e) pure A380 alloy deposit, (b, f) (S) composite deposit, (c, g) (I) composite deposit, and (d, h) (S + I) composite deposit.



**Fig. 6.** Average grain size of A380 matrix in different samples for as-sprayed and heat-treated conditions.

the as-sprayed A380 deposit. However, the local strains were mostly concentrated near the  $\text{Al}_2\text{O}_3/\text{A380}$  interface in the composite samples, thus indicating that  $\text{Al}_2\text{O}_3$  particulates exerted a significant effect on plastic deformation of A380 particles during the spraying process. Further, the local strains disappeared (as evident from the dominant blue shades in Fig. 7(e–h)) after the heat-treatment due to the recovery and re-crystallization phenomena (discussed in section 4).

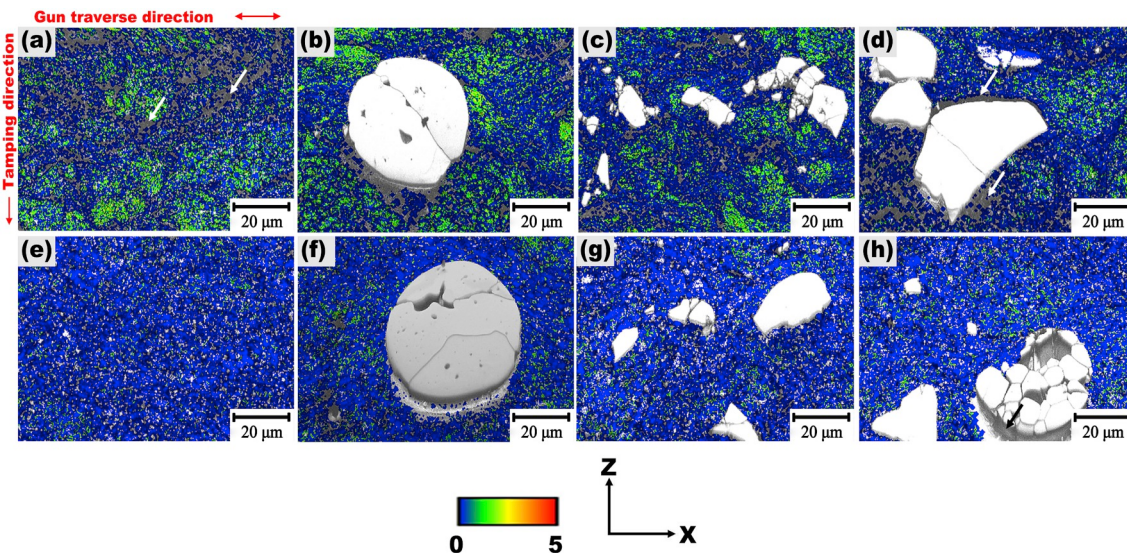
### 3.2. Mechanical properties

Fig. 8 presents the representative stress-strain curves for as-sprayed and heat-treated samples. The as-sprayed samples exhibited brittle tensile behavior with high strength and almost zero plasticity before fracture (Fig. 8(a)). This behavior could be attributed to the severe work hardening effect induced by the CS process. Further, the results indicated that addition of  $\text{Al}_2\text{O}_3$  particulates significantly increased the strength of the materials. The (S) composite deposit displayed the highest strength (~390 MPa) while the (I) and (S + I) composite deposits exhibited slightly lower strengths (~330 MPa). This is due to the severe fragmentation of the irregular  $\text{Al}_2\text{O}_3$ , resulting in the formation of

number of small sized  $\text{Al}_2\text{O}_3$  fragments together with the creation of a large number of  $\text{Al}_2\text{O}_3/\text{A380}$  interfaces. The  $\text{Al}_2\text{O}_3/\text{A380}$  interface bonding is weak in nature, therefore, it is more vulnerable to break/de-bond under the tensile loading. With the continuous application of the load, micro-cracks are generated and propagated at the de-bonded interfaces. However, the strength of (I) and (S + I) composite deposits was still significantly higher than that of the pure A380 alloy deposit (~230 MPa). Heat-treatment generally resulted in reduced ultimate tensile strength and enhanced plasticity of all samples. Deposits containing spherical  $\text{Al}_2\text{O}_3$  particles, i.e., (S) and (S + I) composites, exhibited better mechanical properties. For example, the (S) composite deposit indicated a good combination of mechanical properties, especially a plasticity value of up to 7%, which was significantly higher than that of the other deposits. Mechanical performance of the (S + I) composite deposit (strength and elongation of 225 MPa and 3.5%, respectively) was only lower than that of the (S) deposit. The (I) deposit exhibited poor mechanical properties with its strength (210 MPa) and elongation (1.2%) even lower than those of the A380 deposit (215 MPa and 2.6%, respectively).

Figs. 9 and 10 present the fracture morphologies of as-sprayed and heat-treated samples, respectively. The results indicated that particles in the as-sprayed A380 alloy deposit underwent insufficient deformation during the spraying process. Consequently, severely deformed ellipsoidal particles as well as a few small-sized particles surrounded by large-sized pores were observed (Fig. 9(a–b)). Fracture surface of the (S) composite deposit appeared to be denser than that of the A380 alloy deposit. Due to high degree of deformation of the particles, large-sized pores were virtually invisible (Fig. 9(c–d)). However, the splat boundaries (which acted as nucleation sites for cracks) were clearly visible and the final fracture occurred along these splat boundaries. The (I) and (S + I) composite deposits were not only characterized by splat boundaries of A380 alloy particles but also a large number of weak bonded  $\text{Al}_2\text{O}_3/\text{A380}$  interfaces.

Heat-treatment resulted in dimple-like structures in all four deposits. The heat-treated pure A380 alloy deposit indicated replacement of most well-bonded areas with the dimple-like structure, although some poorly bonded areas were still clearly visible (Fig. 10(b)). The dimples were uniformly distributed over the entire fracture surface in the heat-treated (S) composite deposit. Further, two well-bonded splats fused together after the heat-treatment (red arrows and inset with red border in Fig. 10(d)). Moreover, the  $\text{Al}_2\text{O}_3/\text{A380}$  interface bonding was enhanced as suggested by the absence of a gap in the high magnification SEM



**Fig. 7.** KAM maps of the different samples for as-sprayed and heat-treated conditions: (a, e) pure A380 alloy deposit, (b, f) (S) composite deposit, (c, g) (I) composite deposit, and (d, h) (S + I) composite deposit.

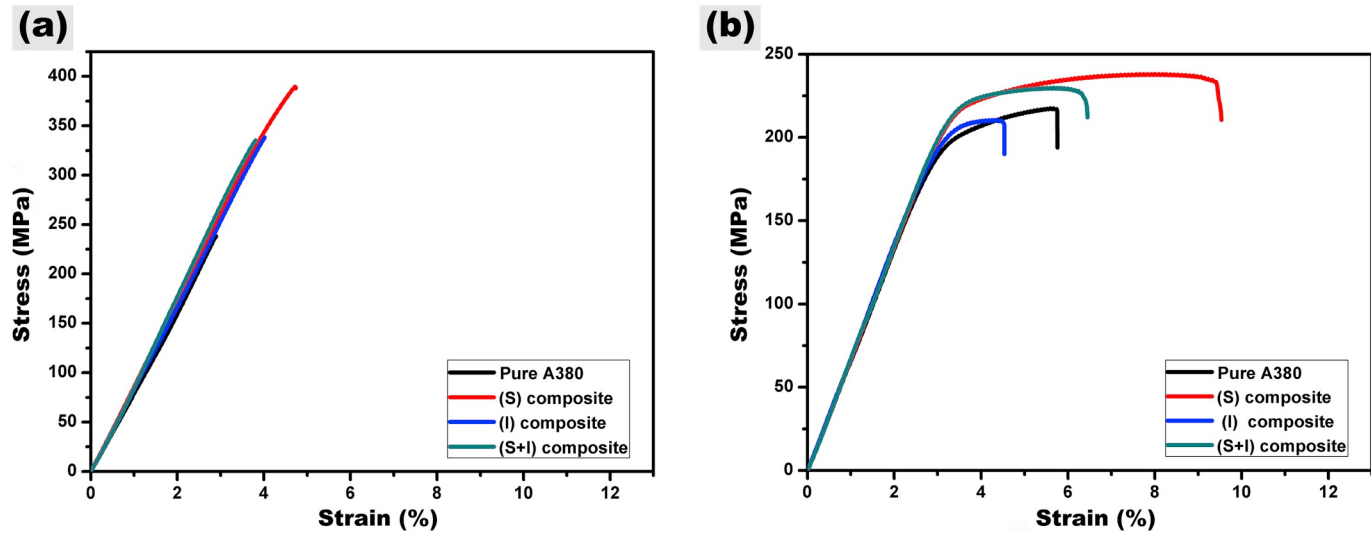


**Fig. 8.** Representative room temperature tensile stress-strain curves for as-sprayed (a) and heat-treated (b) samples.

micrograph (insert with yellow border in Fig. 10(d)). In case of the heat-treated (I) composite deposit, the matrix was mostly covered with dimples and cracks inside the  $\text{Al}_2\text{O}_3$  particles remained unchanged (white arrows in Fig. 10(f)). The  $\text{Al}_2\text{O}_3/\text{A380}$  interfaces were partially healed while most of the interfaces were found to co-exist with micro-defects (gaps, pores, etc.). The fractured surface of the heat-treated (S + I) composite deposit exhibited the characteristics similar to those of the (I) deposit albeit with fewer events of micro-defects.

#### 4. Discussion

The results of this study indicated that (i) the morphology of  $\text{Al}_2\text{O}_3$  particles significantly affected the microstructure and mechanical properties of the cold spray additively manufactured deposits and (ii) the post-spray heat-treatment improved the splat bonding and ductility of samples.

#### 4.1. Effects of $\text{Al}_2\text{O}_3$ particulate morphology

A dense microstructure ensures good physical and mechanical properties of the deposit during cold spraying. These properties in turn depend on sufficient plastic deformation of the metallic particles and the resulting inter-splat bonding. It is well established that feedstock particles accelerated by helium gas can achieve extremely high velocities, thereby increasing the driving force for plastic deformation [27]. However, helium is expensive and thus not an optimal choice for mass scale production of engineering components. Therefore, low-cost nitrogen was used as the working gas in this study. Moreover, hard  $\text{Al}_2\text{O}_3$  particulates were strategically added to the A380 alloy feedstock powder to promote high plastic deformation of the metallic phase through continuous tamping of the pre-deposited layers during cold spraying.

During the CS process, spherical  $\text{Al}_2\text{O}_3$  particulates indicated a more pronounced tamping effect attributed to hitting the pre-deposited layer at a high speed. Getu et al. [28] concluded that the curvature of the spherical  $\text{Al}_2\text{O}_3$  particle boundary remained constant; therefore, elastic rebound forces perpendicular to the impact direction were high enough

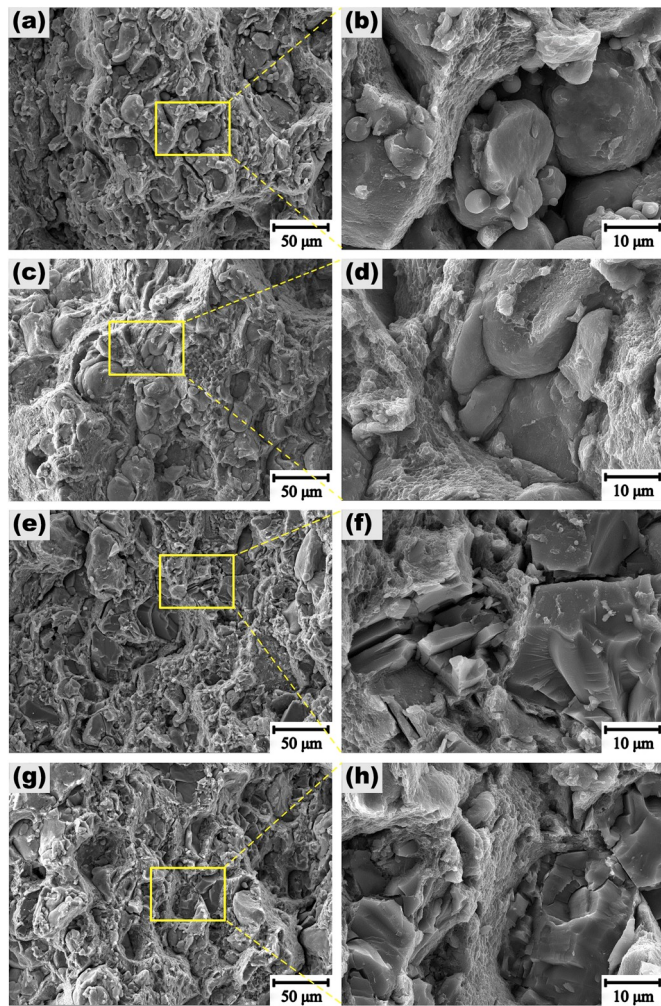


**Fig. 9.** SEM images of fractured surfaces of as-sprayed samples at different magnifications: (a, b) pure A380 alloy deposit, (c, d) (S) composite deposit, (e, f) (I) composite deposit, and (g, h) (S + I) composite deposit.

to prevent embedding of the particles. Thus, spherical particles could be embedded only when they impacted upon the substrate to a depth significantly greater than their radius and were subsequently covered by the in-coming metallic matrix particles. Therefore, most spherical particulates rebounded after transferring a part of their energy to the pre-deposited A380 particles which acted as a driving force for secondary plastic deformation. This is evident from the IPF maps (Fig. 5) which indicate that the matrix grains were deformed and refined throughout the composite deposits. Consequently, the compactness of the whole deposits was enhanced, as evidenced by the improved inter-splat bonding (Fig. 2) and the reduced porosity (Fig. 4) in the as sprayed composites. Moreover, the degree of work hardening of deposits was also improved. Therefore, the strength of deposits containing spherical Al<sub>2</sub>O<sub>3</sub> particles was significantly improved.

In contrast, the irregular Al<sub>2</sub>O<sub>3</sub> particles exhibited a weak tamping effect and dominant embedding effect. Getu et al. [28] reported that the directions of normal and tangential components of elastic rebound forces remained constant for irregular Al<sub>2</sub>O<sub>3</sub> particles which could be attributed to their sharp corners and flat sides. Hence, irregular particles were easy to embed as long as the static friction forces between the particles and the substrate materials were sufficiently high. This embedding phenomenon throughout the material resulted in secondary plastic deformation in the A380 matrix (Fig. 5). However, the deposits were not effectively compacted albeit the sharp corners and flat sides of Al<sub>2</sub>O<sub>3</sub> particles exerted a certain tamping effect on the matrix.

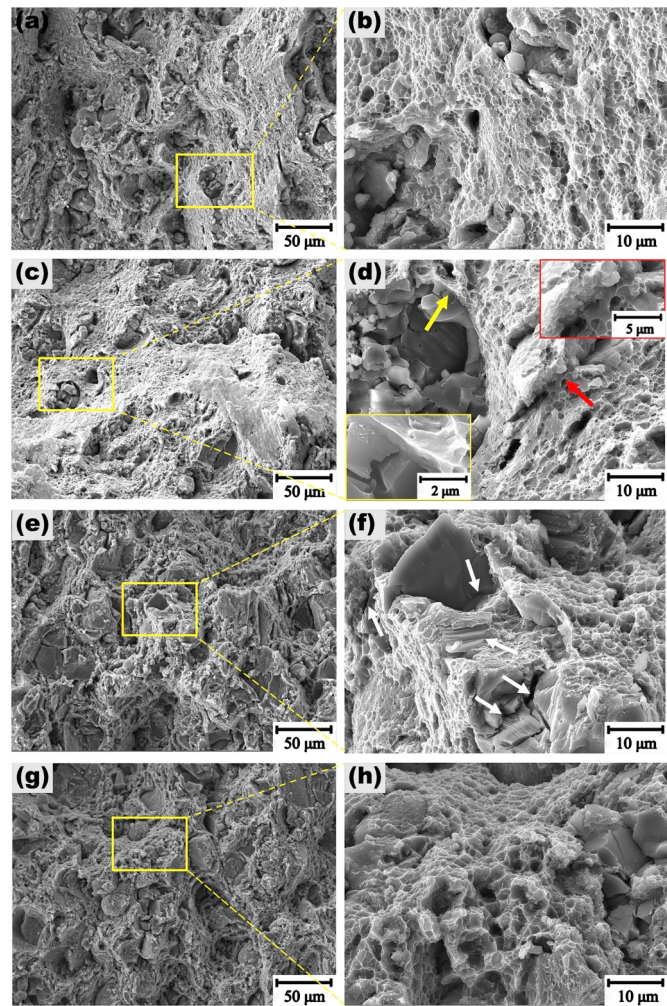


**Fig. 10.** SEM images of fractured surfaces of heat-treated samples at different magnifications: (a, b) pure A380 alloy deposit, (c, d) (S) composite deposit, (e, f) (I) composite deposit, and (g, h) (S + I) composite deposit.

Therefore, the defects located at the splat boundaries were not efficiently eliminated. The addition of irregular Al<sub>2</sub>O<sub>3</sub> particles affected the mechanical properties of the material as follows. Firstly, the Al<sub>2</sub>O<sub>3</sub> particles remained within the deposit to allow the reinforcing (load bearing) of the composite material and improve the strength of the composites. Secondly, the severe fragmentation of the irregular Al<sub>2</sub>O<sub>3</sub> resulted in the formation of a large number of Al<sub>2</sub>O<sub>3</sub>/A380 interfaces. The resulting Al<sub>2</sub>O<sub>3</sub>/A380 interfacial bonding was poor in nature, thus promoting the nucleation of micro cracks. These micro cracks continuously grew under the applied load and resulted in the final breakdown of the material along the Al<sub>2</sub>O<sub>3</sub>/A380 interfaces.

#### 4.2. Influence of post-spray heat-treatment

As discussed in section 3.2, although post-spray heat-treatment resulted in relatively low strength, it significantly enhanced the ductility in all deposits. The influence of heat-treatment on the microstructure and mechanical properties of the cold sprayed samples was affected by (i) improvement in the inter-splat bonding and (ii) recovery and recrystallization phenomena.

##### 4.2.1. Improvement in inter-splat bonding

Previous studies [15–17] have indicated that heat-treatment can heal out defects/pores in cold sprayed deposits and result in improved mechanical properties. In this study, in-situ XCT observation of pores

before and after heat-treatment was conducted (for example, observations for (S) composite deposit are presented in Fig. 11) to elucidate the effects of heat-treatment on internal pores of different deposits. Fig. 11 (a–c) presents the pore details at a certain position in the as-sprayed sample while Fig. 11(d–f) presents pore details at the same position after heat-treatment. The results suggest that a few small-sized pores in the deposit disappeared (white arrow in Fig. 11(b)) while some relatively large-sized pores increased in size (as indicated by color change of pores in Fig. 11(b and d)) after the heat-treatment. The morphological changes in pores are highlighted by rectangles in Fig. 11(b) and (e) and magnified in Fig. 11(c) and (f). After heat-treatment, the pores moved towards each other and were augmented to form a large-sized pore. This suggests that nano-scale pores were located at the splat boundaries of as-sprayed deposits and could not be identified due to limitations of the XCT resolution. The reduction in surface energy during heat-treatment resulted in spheroidization and augmentation of the pores. Consequently, relatively large-sized pores were formed which were easily detected by the XCT, thus indicating slightly higher porosity of the heat-treated samples (Fig. 4). This is consistent with Luo et al. [11] who concluded that the porosity of heat treated Inconel 718 alloy deposits was higher than that of the as-sprayed deposits due to clustering of the two-dimensional tiny inter-particle gaps. The augmentation of pores minimized the proportion of poorly bonded splats and fused the splat boundaries through metallurgical bonding. This observation is consistent with the formation of dimple-like structures on the fracture surfaces of heat treated samples (Fig. 10).

#### 4.2.2. Recovery and re-crystallization

The deposited particles underwent severe plastic deformation during the cold spraying process to result in high dislocation density in the deposits. Consequently, the as-sprayed deposits were characterized by high strength and almost zero ductility. In contrast, heat-treatment effectively eliminated local strains and promoted evolution of fine grains in the as-sprayed deposits through recovery and re-crystallization mechanisms. Consequently, the ductility of the deposits significantly improved. Fig. 12 presents the TEM bright field images to elucidate the microstructure evolution of the (S) composite deposit for as-sprayed and heat-treated conditions.

Fig. 12(a) presents the bonding area of two adjacent A380 splats in the as-sprayed (S) composite deposit. The presence of a deformed strip (width = 1–2  $\mu\text{m}$ ; demarcated by red dotted lines in Fig. 12(a)) indicated that inter-splat bonding was achieved through plastic deformation of the

A380 particles. The magnified image of the deformed strip indicated that it was composed of several highly deformed elongated grains surrounded by regions of high dislocation density (Fig. 12(b)). The select area electron diffraction pattern for the same region exhibited a disrupted ring like feature which corresponded to the presence of numerus nano-sized grains attributed to the continuous occurrence of the dynamic re-crystallization phenomenon [29]. Fig. 12(c) presents the magnified view of the internal region of the splat (yellow border in Fig. 12(a)). The grains in the inner region of the particle maintained their initial equiaxed morphology and larger size. The presence of relatively few dislocation networks in the grain interior indicated that the grain underwent a lower degree of plastic deformation in the central region. This observation is consistent with the EBSD observations (Fig. 5(b)).

In contrast, heat-treatment resulted in an entirely different microstructure. The dislocation density in the deposit was significantly reduced (Fig. 12(d)). This is in accordance with the results obtained from the KAM maps of the heat-treated (S) composite sample (Fig. 7(f)). The aforementioned deformed strips (formed between the two particles) were replaced by a 100 nm long metallurgically bonded zone which comprised nano-sized equiaxed grains (Fig. 12(e)). Moreover, ultrafine grains nucleated at grain boundaries in the inner region of the particles (Fig. 12(f)). This indicates that the CS-induced work hardening and intensive plastic deformation in the deposits gradually recovered due to the static re-crystallization (SRX) phenomenon during the heat-treatment [17]. The strain-free SRXed grains grew further and resulted in an equiaxed grain structure, thereby reducing the stored energy (cold working) of the material. Consequently, the mechanical properties of the material were improved.

## 5. Conclusions

This study demonstrated that the microstructure (splat bonding, pores, dislocations, and grains) of the CSAM-fabricated A380 alloy deposits could be comprehensively adjusted through a combination of (i) addition of dissimilar  $\text{Al}_2\text{O}_3$  particles and (ii) post-spray heat-treatment. The main conclusions of this study are as follows:

1. Spherical  $\text{Al}_2\text{O}_3$  particles exhibited severe tamping effect during the deposition process. Consequently, the (S) composite deposit indicated significantly reduced porosity ( $\sim 0.65\%$ ), low  $\text{Al}_2\text{O}_3$  deposition efficiency, refined average grain size ( $<0.7 \mu\text{m}$ ), and a 70% increase

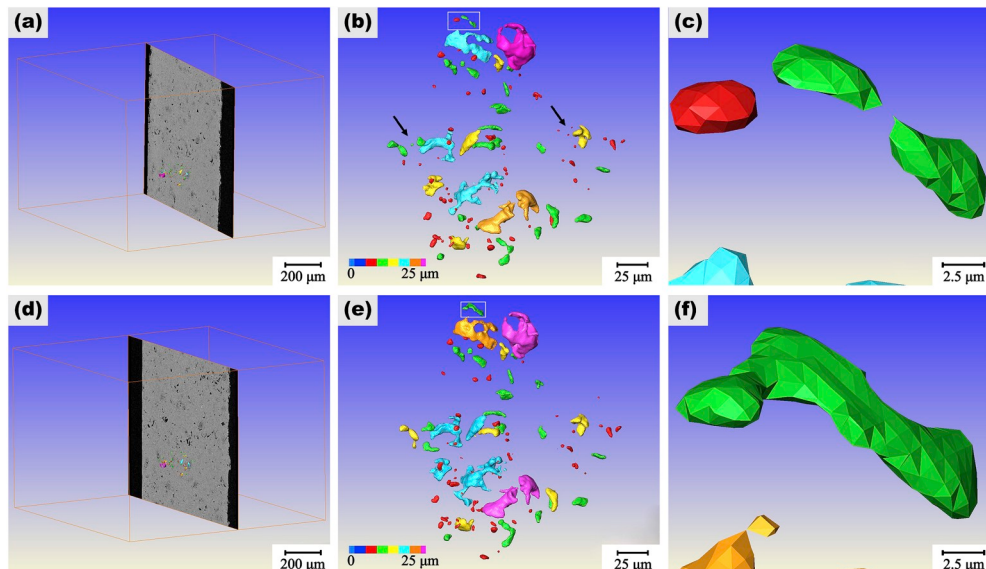


**Fig. 11.** In-situ XCT observation of the evolution of pores in the (S) composite deposit for (a–c) as-sprayed and (d–f) heat-treated conditions.

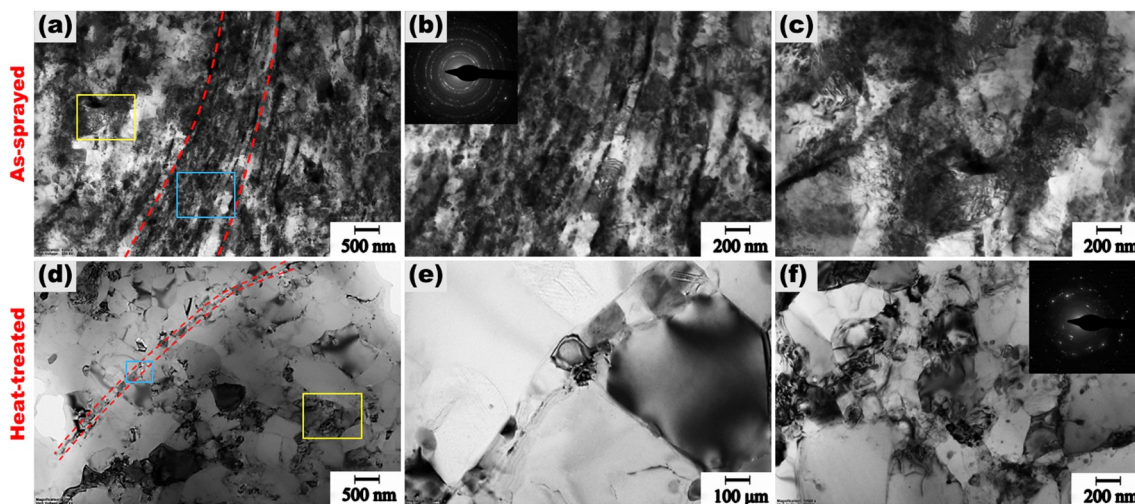


**Fig. 12.** TEM images indicating microstructure evolution in the (S) composite deposit for (a–c) as-sprayed and (d–f) heat-treated conditions.

in the strength (~390 MPa) in contrast to the pure A380 alloy deposit (~230 MPa). Contrarily, the tamping effect of irregular  $\text{Al}_2\text{O}_3$  particles was very weak while the embedding effect was dominant during the CS process. The (I) deposit indicated slightly low porosity (~1.15%) and average grain size (>0.7  $\mu\text{m}$ ) with a 40% increase in strength (~330 MPa) in contrast to the pure A380 alloy deposit. This could be attributed to the fragmentation of  $\text{Al}_2\text{O}_3$  particles and the resulted large amount of weakly bonded  $\text{Al}_2\text{O}_3/\text{A380}$  interfaces inside the deposit.

2. The post-spray heat-treatment resulted in relatively low strength but significantly enhanced ductility in all deposits. This was attributed to improvement in inter-splat bonding and the recovery and recrystallization phenomena. After heat-treatment, pores at the inter-splat boundaries converged towards each other and augmented to form a large-sized pore. Consequently, the proportion of poorly bonded splats minimized and the splat boundaries were fused through metallurgical bonding. Moreover, work hardening and intense plastic deformation in the deposits were gradually recovered through nucleation of strain-free ultrafine grains at the grain boundaries initiated by the recovery and re-crystallization mechanisms.

#### Authors' Contribution

Tian-Ying Xiong and Ji-Qiang Wang proposed the idea and designed the research plan. X. Qiu and L. Qi performed the experiments and collected the data. Naeem ul Haq Tariq polished the language of this paper. X.Qiu, Naeem ul Haq Tariq and J.Q. Wang analyzed the data and wrote the paper.

#### Declaration of competing interest

The authors declare that they have no known competing financial interests or personal relationships that could have appeared to influence the work reported in this paper.

#### Acknowledgment

This work was supported by the National Natural Science Foundation of China [No. 51671205].

#### References

- [1] J.H. Martin, B.D. Yahata, J.M. Hundley, J.A. Mayer, T.A. Schaedler, T.M. Pollock, 3D printing of high-strength aluminium alloys, *Nature* 549 (2017) 365–369.
- [2] C. Chen, Y. Xie, X. Yan, S. Yin, H. Fukanuma, R. Huang, R. Zhao, J. Wang, Z. Ren, M. Liu, H. Liao, Effect of hot isostatic pressing (HIP) on microstructure and mechanical properties of Ti6Al4V alloy fabricated by cold spray additive manufacturing, *Addit Manuf* 27 (2019) 595–605.
- [3] W. Li, K. Yang, S. Yin, X. Yang, Y. Xu, R. Lupoi, Solid-state additive manufacturing and repairing by cold spraying: a review, *J. Mater. Sci. Technol.* 34 (2018) 440–457.
- [4] W.E. Frazier, Metal additive manufacturing: a review, *J. Mater. Eng. Perform.* 23 (2014) 1917–1928.
- [5] S. Yin, P. Cavaliere, B. Aldwell, R. Jenkins, H. Liao, W. Li, R. Lupoi, Cold spray additive manufacturing and repair: fundamentals and applications, *Addit Manuf* 21 (2018) 628–650.
- [6] T. Peat, A. Galloway, A. Toumpis, P. McNutt, N. Iqbal, The erosion performance of cold spray deposited metal matrix composite coatings with subsequent friction stir processing, *Appl. Surf. Sci.* 396 (2017) 1635–1648.
- [7] H. Assadi, F. Gärtnert, T. Stoltenhoff, H. Kreye, Bonding mechanism in cold gas spraying, *Acta Mater.* 51 (2003) 4379–4394.
- [8] R. Jenkins, S. Yin, B. Aldwell, M. Meyer, R. Lupoi, New insights into the in-process densification mechanism of cold spray Al coatings: low deposition efficiency induced densification, *J. Mater. Sci. Technol.* 35 (2019) 427–431.
- [9] H. Assadi, H. Kreye, F. Gärtnert, T. Klassen, Cold spraying – a materials perspective, *Acta Mater.* 116 (2016) 382–407.
- [10] M.R. Rokni, C.A. Widener, O.C. Ozdemir, G.A. Crawford, Microstructure and mechanical properties of cold sprayed 6061 Al in As-sprayed and heat treated condition, *Surf. Coat. Technol.* 309 (2017) 641–650.
- [11] X.T. Luo, M.L. Yao, N.S. Ma, M. Takahashi, C.J. Li, Deposition behavior, microstructure and mechanical properties of an in-situ micro-forging assisted cold spray enabled additively manufactured Inconel 718 alloy, *Mater. Des.* 155 (2018) 384–395.
- [12] X. Suo, X. Guo, W. Li, M.-P. Planche, R. Bolot, H. Liao, C. Coddet, Preparation and characterization of magnesium coating deposited by cold spraying, *J. Mater. Process. Technol.* 212 (2012) 100–105.
- [13] V. Champagne, D. Helfritch, The unique abilities of cold spray deposition, *Int. Mater. Rev.* 61 (2016) 437–455.
- [14] X. Qiu, N. Tariq, L. Qi, J.-R. Tang, X.-Y. Cui, H. Du, J.-Q. Wang, T.-Y. Xiong, Effects of dissimilar alumina particulates on microstructure and properties of cold-sprayed alumina/a380 composite coatings, *Acta Metall. Sin. -Engl. Lett.* 32 (2019) 1449–1458, <https://doi.org/10.1007/s40195-019-00917-z>.
- [15] R. Huang, W. Ma, H. Fukanuma, Development of ultra-strong adhesive strength coatings using cold spray, *Surf. Coat. Technol.* 258 (2014) 832–841.
- [16] P. Coddet, C. Verdy, C. Coddet, F. Debray, F. Lecouturier, Mechanical properties of thick 304L stainless steel deposits processed by He cold spray, *Surf. Coat. Technol.* 277 (2015) 74–80.
- [17] R. Huang, M. Sone, W. Ma, H. Fukanuma, The effects of heat treatment on the mechanical properties of cold-sprayed coatings, *Surf. Coat. Technol.* 261 (2015) 278–288.
- [18] X. Qiu, J.-q. Wang, N.u.H. Tariq, L. Gyansah, J.-x. Zhang, T.-y. Xiong, Effect of heat treatment on microstructure and mechanical properties of A380 aluminum alloy deposited by cold spray, *J. Therm. Spray Technol.* 26 (2017) 1898–1907.
- [19] K. Spencer, D.M. Fabijanic, M.X. Zhang, The influence of  $\text{Al}_2\text{O}_3$  reinforcement on the properties of stainless steel cold spray coatings, *Surf. Coat. Technol.* 206 (2012) 3275–3282.
- [20] E. Irissou, J.G. Legoux, B. Arsenault, C. Moreau, Investigation of Al-Al $\text{O}_3$  cold spray coating formation and properties, *J. Therm. Spray Technol.* 16 (2007) 661–668.
- [21] Y.Y. Wang, B. Normand, N. Mary, M. Yu, H.L. Liao, Effects of ceramic particle size on microstructure and the corrosion behavior of cold sprayed SiCp/Al5056 composite coatings, *Surf. Coat. Technol.* 315 (2017) 314–325.

- [22] W.Y. Li, G. Zhang, H.L. Liao, C. Coddet, Characterizations of cold sprayed TiN particle reinforced Al2319 composite coating, *J. Mater. Process. Technol.* 202 (2008) 508–513.
- [23] X. Qiu, N.u.H. Tariq, L. Qi, Y.-n. Zan, Y.-j. Wang, J.-q. Wang, H. Du, T.-y. Xiong, In-situ Sip/A380 alloy nano/micro composite formation through cold spray additive manufacturing and subsequent hot rolling treatment: microstructure and mechanical properties, *J. Alloy. Comp.* 780 (2019) 597–606.
- [24] B. Al-Mangour, P. Vo, R. Mongrain, E. Irissou, S. Yue, Effect of heat treatment on the microstructure and mechanical properties of stainless steel 316L coatings produced by cold spray for biomedical applications, *J. Therm. Spray Technol.* 23 (2014) 641–652.
- [25] A.C. Hall, D.J. Cook, R.A. Neiser, T.J. Roemer, D.A. Hirschfeld, The effect of a simple annealing heat treatment on the mechanical properties of cold-sprayed aluminum, *J. Therm. Spray Technol.* 15 (2006) 233–238.
- [26] B. Dikici, H. Yilmazer, I. Ozdemir, M. Isik, The effect of post-heat treatment on microstructure of 316L cold-sprayed coatings and their corrosion performance, *J. Therm. Spray Technol.* 25 (2016) 704–714.
- [27] X.T. Luo, Y.K. Wei, Y. Wang, C.J. Li, Microstructure and mechanical property of Ti and Ti6Al4V prepared by an in-situ shot peening assisted cold spraying, *Mater. Des.* 85 (2015) 527–533.
- [28] H. Getu, J.K. Spelt, M. Papini, Conditions leading to the embedding of angular and spherical particles during the solid particle erosion of polymers, *Wear* 292–293 (2012) 159–168.
- [29] Y. Zou, W. Qin, E. Irissou, J.-G. Legoux, S. Yue, J.A. Szpunar, Dynamic recrystallization in the particle/particle interfacial region of cold-sprayed nickel coating: electron backscatter diffraction characterization, *Scr. Mater.* 61 (2009) 899–902.